



Cite this: *RSC Adv.*, 2020, **10**, 5758

Received 25th December 2019  
 Accepted 31st January 2020

DOI: 10.1039/c9ra10916a

[rsc.li/rsc-advances](http://rsc.li/rsc-advances)

## High dielectric thin films based on barium titanate and cellulose nanofibrils<sup>†</sup>

Jie Tao, <sup>a</sup> Shun-an Cao, <sup>\*a</sup> Rui Feng<sup>b</sup> and Yulin Deng<sup>\*c</sup>

A series of composite films based on tetragonal barium titanate (BTO) and cellulose nanofibrils (CNF) with high dielectric constant are prepared using a casting method in aqueous solution. No organic solvent is involved during the preparation, which demonstrates the environmental friendliness of the novel material. With less than 30 wt% of filler loading, the excellent distribution of BTO nanoparticles within the CNF matrix is revealed by the FE-SEM images. The dielectric constant of the CNF/BTO (30 wt%) composite film reaches up to 188.03, which is about seven times higher than that of pure CNF (25.24), while the loss tangent only rises slightly from 0.70 to 1.21 (at 1 kHz). The thin films kept their dielectric properties on an acceptable level after repeatedly twisting or rolling 10 times. The improvement of thermal stability is observed with the presence of BTO. The outstanding dielectric properties of the CNF/BTO composite film indicates its great potential to be utilized in energy storage applications.

## Introduction

In the past decades, considerable research effort has been made to exploit sustainable energy to replace fossil fuels and reduce pollution.<sup>1</sup> High dielectric materials (HDMs) are of vital importance in energy storage and conversion devices for solar and wind energy because of their high energy density and power density. HDM based capacitors receive much attention in the applications of portable electronics, hybrid electric vehicles, and so on.<sup>2</sup> Excellent HDMs can significantly cut down dissipation, improve the efficiency of energy storage, and shrink the size of devices.<sup>3</sup> Organic/inorganic composites are some of the most extensively studied HDMs as they combine the merits of both components, such as enhanced dielectric properties, outstanding thermal stabilities, bio-compatibility, light weight, low cost and remarkable processing properties.<sup>4–7</sup>

Ferroelectric ceramics such as lead-free barium titanate ( $\text{BaTiO}_3$ , BTO) have long been of interest as fillers for high dielectric composites.<sup>8,9</sup> This is due to their high dielectric constant (as high as 7000),<sup>10</sup> low dissipation, impressive piezoelectric and pyroelectric properties.<sup>11,12</sup> The effects of size, shape (e.g., nanoparticles, nanorods, nanowires, nanocubes), crystal phase (e.g., cubic, tetragonal, orthorhombic, rhombohedral),

matrix, surface conditions, porosity, filler loading and distributions have been discussed intensively in the literature.<sup>13–18</sup> By adjusting these factors, a range of BTO based composites have been reported to have splendid dielectric properties.<sup>19–24</sup> Dang *et al.*<sup>25</sup> modified BTO particles (diameter = 700 nm) with 1.0 wt% of silane coupling agent (KH550) to improve its compatibility with polyvinylidene fluoride (PVDF), and the relative dielectric constant ( $\epsilon_r$ ) of the PVDF/BTO (40.0 vol%) composite (thickness = 1 mm) is more than 50, whereas the loss tangent ( $\tan \delta$ ) is lower than 0.03 (at 1 kHz). In order to improve the thermal stabilities, Dang's research group<sup>26</sup> then prepared polyimide (PI)/BTO composite by *in situ* polymerization. With 40 vol% of BTO (diameter  $\sim$  100 nm) loaded, the  $\epsilon_r$  of the films (thickness 10–70  $\mu\text{m}$ ) reaches 18, while  $\tan \delta$  is below 0.01 (at 1 kHz). More PVDF based polymers are employed as the dielectric matrix, and their  $\epsilon_r$  is in the range from 30 to 50 (at 1 kHz) with  $\tan \delta$  lower than 0.05.<sup>27–29</sup> Kim *et al.*<sup>30</sup> investigated polycarbonate (PC) as the matrix for chemically functionalized BTO and obtained a series of thin films nanocomposite (thickness = 3.89  $\mu\text{m}$ ). With a filler content of 50 vol%, the  $\epsilon_r$  of the sample film is  $37 \pm 2$ , and  $\tan \delta$  is  $<0.03$  (at 1 kHz). Luo *et al.*<sup>31</sup> designed a 3D BTO network and synthesized a composite by injecting epoxy solutions into the porous structure. With 30 vol% BTO (size of grain = 0.5–1  $\mu\text{m}$ ) loaded, a high  $\epsilon_r$  of 200 is achieved with a  $\tan \delta$  of 0.14 (at 1 kHz).

The recent researches based on BTO fillers focus more on improving breakdown strength and reducing  $\tan \delta$  to pursue higher energy density and storage efficiency.<sup>31–38</sup> Generally, most of the applied polymer matrices are non-biodegradable or even toxic. And some of the matrix polymers, such as polycarbonate, reported in the literature are fragile or stiff, which are not suitable for soft and portable electronic applications.

<sup>a</sup>School of Power and Mechanical Engineering, Wuhan University, Wuhan, 430072, China. E-mail: shunancao@163.com

<sup>b</sup>School of Material Science and Engineering, Wuhan University of Technology, Wuhan, 430070, China

<sup>c</sup>School of Chemical & Biomolecular Engineering, Renewable Bioproducts Institute, Georgia Institute of Technology, Atlanta, GA 30332-0620, USA. E-mail: yulin.deng@rbi.gatech.edu

<sup>†</sup> Electronic supplementary information (ESI) available. See DOI: 10.1039/c9ra10916a



Therefore, more and more researchers are exploring safe, green and environmentally friendly alternatives. Cellulose, nanocellulose and their derivatives are reported to be a promising replacement for the traditional polymer dielectric matrices.<sup>39–62</sup> Chiang *et al.*<sup>63</sup> mixed BTO (diameter < 2  $\mu\text{m}$ ) with cyanoethyl cellulose (CEC) in acetone and prepared a well-dispersed composite with a thickness of 100–350  $\mu\text{m}$ . The  $\epsilon_r$  of the composite increases from 21 for pure CEC to 133 (at 1 kHz) with the addition of 51 vol% BTO. Jia *et al.*<sup>64</sup> reported a three-phase composite (thickness  $\sim$  75  $\mu\text{m}$ ) based on 30 wt% BTO (diameter  $\approx$  100 nm), 24 wt% antimony tin oxide (ATO, diameter  $\approx$  10 nm), and CEC. The  $\epsilon_r$  of the CEC/ATO/BTO nanocomposite film reaches 66.08 with a  $\tan \delta$  of  $\sim$  0.1 (at 1 kHz). Cellulose is a common and almost inexhaustible resource in nature. Recently, novel nanocellulose garners attention because of its specific properties such as good dielectric properties, low coefficient of thermal expansion, flexible, excellent mechanical properties, high transparency, low density, and strong chemical durability.<sup>65–74</sup> It is worth to note that nanocellulose is made from pure mechanical grinding, thus no toxic solvent is needed for its production. Hassan *et al.*<sup>11</sup> doped BTO (diameter  $\approx$  180 nm) into 2,2,6,6-tetramethylpiperidinyl-1-oxyl (TEMPO) oxidized cellulose nanofibrils (CNFs). With 5 wt% BTO added, the  $\epsilon_r$  of the composite films of TEMPO-modified CNF (TCNF) and BTO (thickness of 0.09–1 mm) is 49 000, which is four times higher than that of pure TCNF films (11 034 at 1 kHz). And  $\tan \delta$  is increased from  $\sim$  0.01 for pure CNF to  $\sim$  2. In our previous study, titanium dioxide ( $\text{TiO}_2$ ) was used as the filler, and the dielectric properties of CNF/ $\text{TiO}_2$  and TCNF/ $\text{TiO}_2$  nanocomposite were compared.<sup>42</sup> It was found that CNF is a better choice than TCNF as the high dielectric matrix for the sake of reliability and energy saving. With 50 wt% of  $\text{TiO}_2$  loaded, the  $\epsilon_r$  of the CNF/ $\text{TiO}_2$  nanocomposite films is 19.51 with a  $\tan \delta$  of 0.81.

Based on the above discussions, here we report a 0–3 composite high dielectric system by directly mixing zero-dimensional BTO with three-dimensional CNF in aqueous solution. A series of flexible free-standing CNT/BTO nanocomposite films was prepared by casting method and hot-press treatment. We choose isotropic BTO particles as filler due to its simplicity synthesis in practical applications. BTO nanoparticles were thermally treated to get a tetragonal phase, which is reported to have a higher  $\epsilon_r$  than a cubic phase.<sup>18</sup> Theoretically, the positively charged surface of BTO nanoparticles should be able to adhere to the negatively charged surface of CNF.<sup>11</sup> Since both BTO and CNF are highly dispersible in water, no organic solvent was used during the process. Morphologies, phase compositions, dielectric related properties and thermal stabilities of the CNF/BTO sample films were measured and evaluated, and the results demonstrate that the obtained nanocomposite has great potential to be practically utilized in energy storage applications.

## Experimental

### Materials

CNF slurry with a solid content of  $\sim$  3% was supplied by Cellulose Lab Inc. (Canada) and used as received.<sup>75–78</sup> The CNF has

a diameter of 6–80 nm with a length of several micrometers.  $\text{BaTiO}_3$  nanoparticles (diameter  $<$  100 nm, 99.9%) was purchased from Aladdin Co., Ltd. (China), and calcined at 1000 °C for 10 hours. Deionized water was obtained by a Millipore Direct-Q3 water purification system.

### Sample preparation

The CNF/BTO nanocomposite films were prepared by simply mixing and solution casting method, as shown in Fig. 1. The CNF/BTO nanocomposite films were prepared by simply mixing and solution casting method, as shown in Fig. 1. CNF slurry was diluted into 0.3 wt% by deionized water, and stirred by a homogenizer (RCD-1A, Changzhou yuexin, China) for 5 min. After the dilution, a certain amount of BTO was added according to the dry weight percentage, and the solution was homogenized for 5 min again. Subsequently, the solution was poured into a Petri dish and dried in a fume hood for several days. Finally, the obtained film was hot-pressed under 80 °C for 3 hours. The thickness of the flexible films was in the range of 30–100  $\mu\text{m}$ .

### Measurement and characterization

The surface and cross-section morphologies of sample films were investigated by field-emission scanning electron microscopy (FE-SEM, TESCAN MIRA3, Czech Republic) with an accelerating voltage of 5 kHz. Prior to the measurement, the samples were coated with a thin layer of gold using a sputter coater (Quorum SC7620, UK) in a vacuum to reduce charge interruptions. Energy-dispersive X-ray spectroscopy (EDS, Oxford X-Max20, UK) was used to analyze the distribution of BTO in the CNF matrix. X-ray diffraction (XRD) patterns of BTO particles and CNF/BTO composite films were determined by an X-ray diffraction spectrometer (XRD, PANalytical XPert Pro, Netherlands). The XRD patterns were recorded with  $\text{Cu K}_\alpha$  radiation ( $\lambda = 1.542 \text{ \AA}$ ) at 40 kV and 40 mA in the 2 theta ( $2\theta$ ) value range from 5° to 80°. The thermal stabilities of the nanocomposites were tested by thermogravimetric analysis and differential scanning calorimetry (TGA-DSC, Netzsch STA449F3, Germany) at a heating rate of 10 °C min<sup>−1</sup> from 35 °C to 790 °C under a nitrogen atmosphere. The dielectric constant, loss tangent and AC electrical conductivity of sample films were studied using an LCR meter (Keysight E4980A, USA). The results were

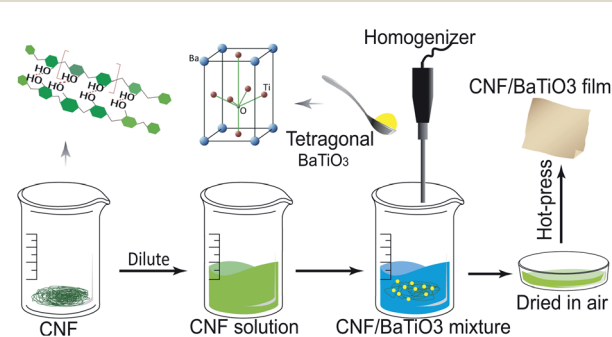


Fig. 1 Preparation of CNF/BTO nanocomposite films.



recorded in the frequency range from 40 Hz to 1 MHz with an oscillation signal of 1 V at ambient temperature. Prior to the measurement, gold electrodes were sputtered on both sides of the specimens, and the test was repeated four times for each composition. The relative dielectric constants ( $\epsilon_r$ ) of the sample films were calculated by eqn (1):

$$\epsilon_r = \frac{C \times d}{A \times \epsilon_0} \quad (1)$$

where,  $C$  is the capacitance;  $\epsilon_0$  is the absolute dielectric constant of vacuum,  $\epsilon_0 = 8.854 \times 10^{-12} \text{ F m}^{-1}$ ;  $A$  is the electrode area,  $A = 4.52 \times 10^{-6} \text{ m}^2$ ;  $d$  is the thickness of the sample film. The polarization–electric field ( $P$ – $E$ ) curves of the sample films were measured with a ferroelectric tester (Radian Precision Multi-ferroic II, USA) at 100 Hz.

## Results and discussion

### Morphology

Well dispersion of BTO filler is conducive to uniform packing of CNF/BTO nanocomposite, leading to better dielectric properties. The surface and cross-section morphologies of the pure CNF and CNF/BTO composite films were investigated by FE-SEM images (shown in Fig. 2). Pure CNF film had a smooth surface and laminated structure (Fig. 2a and d). The morphological changes induced by BTO fillers on the CNF are very clear. In the lower range of filler content, BTO particles exhibited good dispersion in the CNF matrix, in turn, the composite films kept as dense as pure CNF film. With the addition of 30 wt% BTO, small voids and a rough surface started to be seen due to the aggregation of BTO (Fig. 2b and e). BTO particles with a diameter of 0.5–1.0  $\mu\text{m}$  are resulted from high-temperature calcination, and there are strong forces between particles.<sup>79</sup> Generally,

BTO particles are still uniformly dispersed throughout the CNF matrix, which is in good accordance with EDS results (Fig. S1–S6†). In the specimens with higher BTO content, the laminated structure disappeared, and big spheres with a diameter of >10  $\mu\text{m}$  are observed (Fig. 2c and f). The films exhibit porous and loose structure due to the weakening of CNF chain–chain interactions by the inclusion of BTO particles.<sup>79</sup> This result shows that uniform CNF/BTO nanocomposite films can be obtained by simple mechanical mixing and casting methods when filler content below 30 wt%.

### Phase composition

The dielectric properties of the composite are influenced by the crystal properties of the constituents. Tetragonal BTO has a higher dielectric constant than other phases, *e.g.*, cubic phase. Taking this advantage, tetragonal BTO has much higher commercial value than other phases. The phase compositions of pure CNF, untreated BTO, thermally treated BTO, and CNF/BTO (30 wt%) composites were recorded by XRD patterns, as is presented in Fig. 3. The broad peak in the region of 15° to 17° and at 22.6° are corresponding to the partly crystalline structure of CNF.<sup>11,62,80</sup> The peak intensity of CNF in the nanocomposite films decreased with the addition of BTO due to the destruction of the ordered structure.<sup>64</sup> The XRD pattern of thermally treated BTO was in line with tetragonal BTO (JCPDS No. 89-1428). Especially, the characteristic splitting peak of the tetragonal phase was seen distinctively at 45°.<sup>79,81,82</sup> Owing to the higher crystallinity of BTO, its peaks were much sharper than that of CNF. In the XRD pattern of CNF/BTO composite, the peak intensity of both CNF and BTO decreased compared with pure CNF and BTO. It is ascribed to the addition of nanofillers, which destroys the ordered structure of the CNF and reduces its

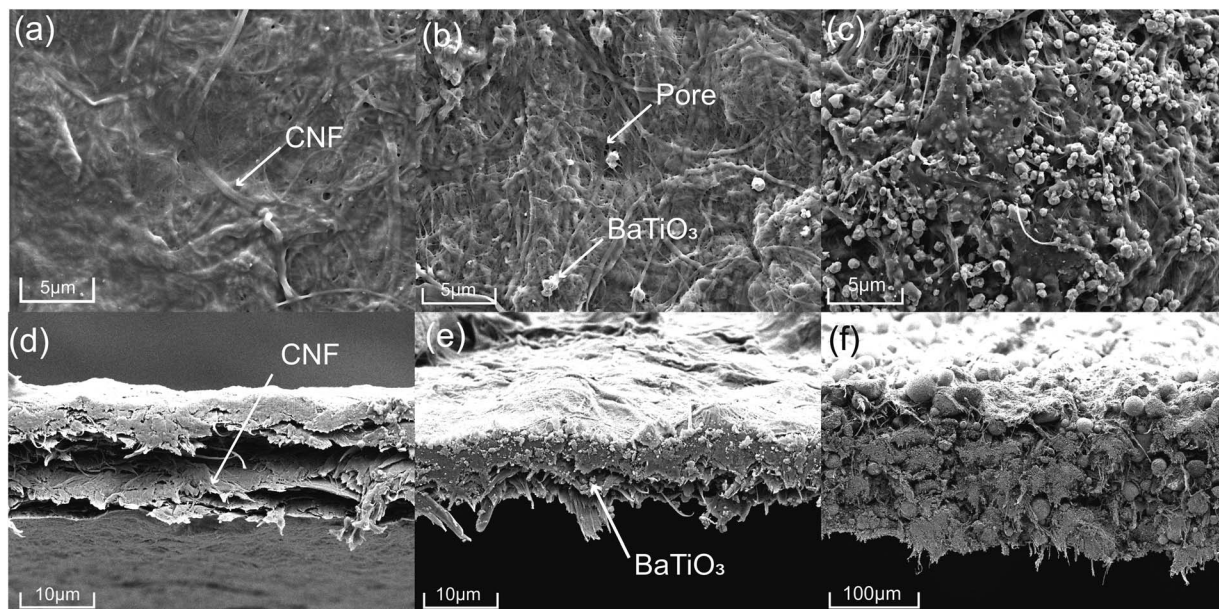


Fig. 2 Surface and cross-section FE-SEM micrographs of pure CNF (a and d), CNF/BTO (30 wt%) (b and e) and CNF/BTO (90 wt%) (c and f) composite films.



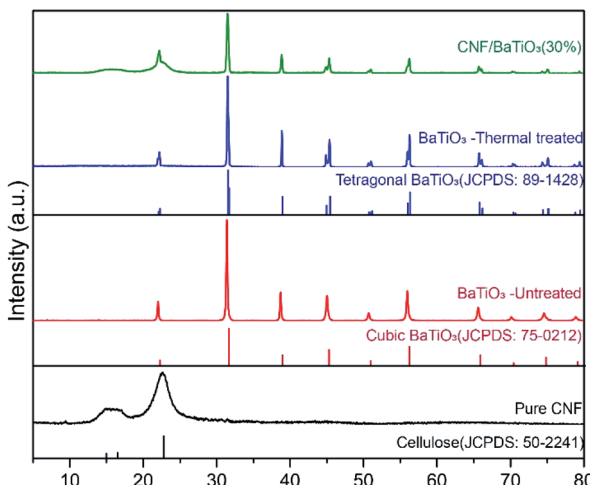


Fig. 3 XRD patterns of pure CNF, untreated BTO, thermally treated BTO, and CNF/BTO (30 wt%) nanocomposite films.

crystallinity.<sup>83</sup> It is worth mentioning that the peak positions of both CNF and BTO remained unchanged in the CNF/BTO composite, which indicates that the mechanical mixing process does not affect the crystalline structure of these two constituents.<sup>61</sup>

### Dielectric properties

The dielectric properties usually refer to the relative dielectric constant ( $\epsilon_r$ ) and loss tangent (dissipation factor,  $\tan \delta$ ). Towards the application of energy storage, conductivity and  $P$ - $E$  hysteresis loop were also examined. All of these properties are considerably affected by the frequency. The frequency dependence of  $\epsilon_r$  and  $\tan \delta$  was studied, as shown in Fig. 4a and b. In the low-frequency range of 40–10 kHz, both  $\epsilon_r$  and  $\tan \delta$  decreased sharply with the increase of frequency, and a  $\tan \delta$  peak was presented in the plot of samples with 0–40 wt% BTO. These are typical characteristics of electrode effect and Maxwell–Wagner–Sillars interfacial polarization.<sup>50,60,84–86</sup> With the frequency going up, the high periodic reversal of the electric field makes it harder for dipoles and charge carriers, which accumulated at the interface, to catch up with the change of frequency. Hence, the interfacial polarization is decreased and results in lower  $\epsilon_r$  and  $\tan \delta$ .<sup>87</sup>

In the meantime,  $\epsilon_r$  increases with filler content before 30 wt% and decreases with the further addition of BTO. It can be explained by Tanaka's model, which assumes that the interface of a filler particle consists of three layers: a bonded layer, a bound layer, and a loose layer. Additionally, there is an electric double layer overlapping the above three layers.<sup>88</sup> Reducing the particle size of BTO to the nanoscale, as well as increasing BTO loading, offers larger surface areas for interfacial polarization, resulting in an extraordinary increase of both  $\epsilon_r$  and  $\tan \delta$ .<sup>72</sup> However, at the same time, the bonded layer and bound layer of the nanoparticles impair the motion of dipoles and leads to a decrease of  $\epsilon_r$  and  $\tan \delta$ . Besides, the response of dipoles and ionic carriers in the loose layer is more

complicated. Coincidentally, BTO aggregations started to be seen with a filler content of 30 wt% in FE-SEM images. It can be ascribed to the far-field effect of the double electric layer, which makes the loose layers of neighbored nanoparticles collaborate with each other. On the one hand, the resulted imperfection of heterogeneous structures helps to improve  $\epsilon_r$  and  $\tan \delta$ . On the other hand, the porous structure brought by severe aggregation can dramatically cut down  $\epsilon_r$  and  $\tan \delta$ .

In the higher frequency range of above 100 kHz,  $\epsilon_r$  and  $\tan \delta$  were almost insusceptible to the frequency and remains constant. It illustrates that electronic polarization, atomic polarization, and orientation polarization starts to play a predominant role. In this frequency range, filler content also has no obvious influence on  $\epsilon_r$  and  $\tan \delta$ . The  $\epsilon_r$  of CNF/BTO composite films reaches its maximum value of 188.03 with 30 wt% of BTO, which is more than seven times higher than that of pure CNF, whose  $\epsilon_r$  is 25.24 (at 1 kHz). Meanwhile, the  $\tan \delta$  is only slightly grown from 0.70 to 1.21 (at 1 kHz). The dielectric constant of CNF/BTO composite is competitive with other BTO based composites, whose  $\epsilon_r$  is in the range from 30 to 50,<sup>25–30</sup> and cellulose-based composites, whose  $\epsilon_r$  is lower than 135.<sup>63,64</sup> However, similar to most of other dielectric composites, higher  $\epsilon_r$  is accompanied with higher  $\tan \delta$ . Therefore, more efforts to decrease the loss tangent is still needed. In general, the outstanding dielectric properties of CNF/BTO nanocomposite film render it a promising candidate for capacitor applications.

To further explore the electric properties of CNF/BTO (30 wt%) nanocomposites, the frequency dependence of AC conductivity ( $\sigma_{AC}$ ) was tested and compared with pure CNF (as shown in Fig. 4c). The  $\sigma_{AC}$  of both samples ascended with the increase of frequency. In the lower frequency range of 40 Hz to 100 kHz, the trend was gradual, while it turned rapidly with the frequency further increased. This phenomenon complies well with Dyre's random free energy barrier model.<sup>89</sup> The frequency-dependent property of  $\sigma_{AC}$  is related to the hopping of the charge carriers in the localized state and upper states in the conduction band. And this process can be accelerated by higher frequency.<sup>11,61</sup> Composite films with 30 wt% BTO exhibited higher  $\sigma_{AC}$  than that of pure CNF. It is attributed to its higher crystallinity, as evidenced by XRD patterns. Besides, the integration of BTO in CNF piles up more interfacial areas and charges, resulting in higher  $\sigma_{AC}$ . At 1 kHz, the  $\sigma_{AC}$  increased from  $3.15 \times 10^{-7} \text{ S cm}^{-1}$  for CNF to  $1.07 \times 10^{-6} \text{ S cm}^{-1}$  for CNF/BTO (30 wt%).

The polarization–electric field ( $P$ - $E$ ) hysteresis curve is an efficient way to evaluate the energy storage properties. The  $P$ - $E$  hysteresis curves of pure CNF and the CNF/BTO (30 wt%) were measured, as shown in Fig. 4d. Both remnant polarization ( $P_r$ ) and saturated polarization ( $P_s$ ) of CNF/BTO composite films were higher than that of pure CNF. It demonstrates that the addition of BTO makes it easier to be polarized, which is also proved by the results that CNF/BTO composite has a higher  $\epsilon_r$  than that of pure CNF. However, the  $P_r$  of the composite film was very close to  $P_s$ , suggesting a low efficiency of energy storage.<sup>11</sup> The polarization of CNF/BTO film saturated before the electric field reached its maximum value. It may be caused by the leakage current which is the result of a heterogeneous



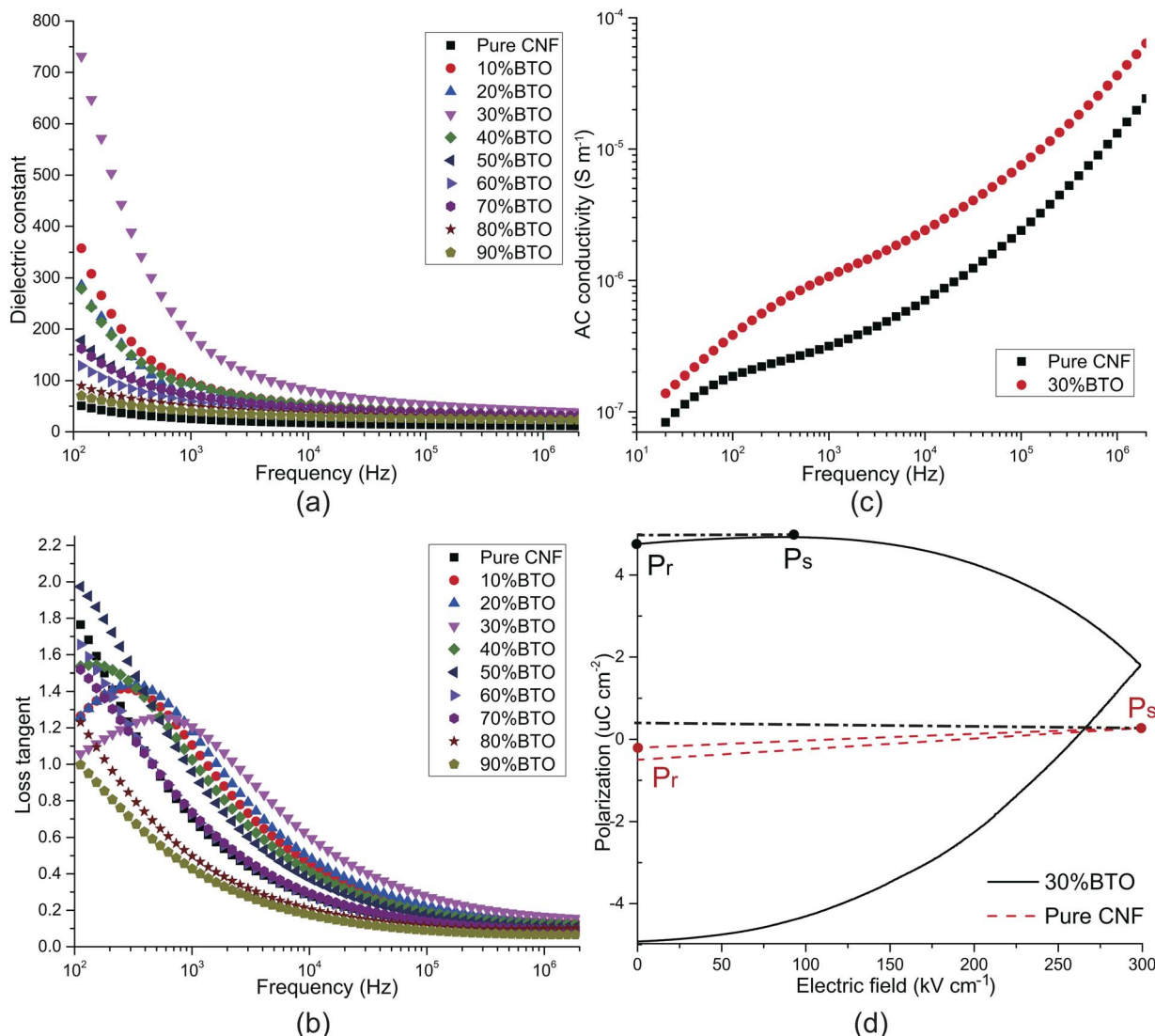


Fig. 4 Dielectric properties of CNF/BTO nanocomposite films. The influence of frequency and filler content on the (a) dielectric constant, (b) dielectric loss, and (c) AC conductivity (d)  $P$ - $E$  hysteresis curves of CNF/BTO nanocomposites.

structure. In order to be utilized in the area of energy storage application, more efforts should be made on improving the dispersion of BTO fillers and reducing the remnant polarization.

#### Influence of twisting treatments

In order to study the potential of this high dielectric film as a soft electronic material, the dielectric properties of CNF/BTO (30 wt%) nanocomposite after being repeatedly twisted into a roll (CNF/BTO-R) and ball (CNF/BTO-B) for 10 times, and their dielectric properties were measured again, as shown in Fig. 5. Though both the  $\epsilon_r$  and  $\tan \delta$  decreased after the rolling treatment. The  $\epsilon_r$  for untreated CNF/BTO, CNF/BTO-R, and CNF/BTO-B are 129.56, 90.58, and 43.44, respectively, while the  $\tan \delta$  are 1.07, 0.65, and 0.51, respectively. The CNF/BTO-B films exhibited lower  $\epsilon_r$  and  $\tan \delta$  than that of CNF/BTO-R, which might be caused by more air being entrapped in the

film during the twisting or rolling process. This was proved by the observation of the rougher surface and higher thickness (by  $\sim 5\%$ ) of CNF/BTO-B. It is worth to note that the rolled CNF/BTO-B films still showed higher dielectric properties compared with other reported composites.<sup>42</sup> And at high frequency, the difference of  $\epsilon_r$  and  $\tan \delta$  between these samples are much smaller, which suggests the possibility of the flexible CNF/BTO film to be utilized in the high-frequency applications such as antenna.

#### Thermal stability

In practical application, thermal stability is one of the most important concerns. The TGA-DSC curve of CNF/BTO (30 wt%) composite film was measured, as depicted in Fig. 6. Two steps were presented in the degradation process. The first degradation step is the slight weight loss before 100 °C, resulting from the evaporation of moisture.<sup>42</sup> The temperature at 5.0% weight



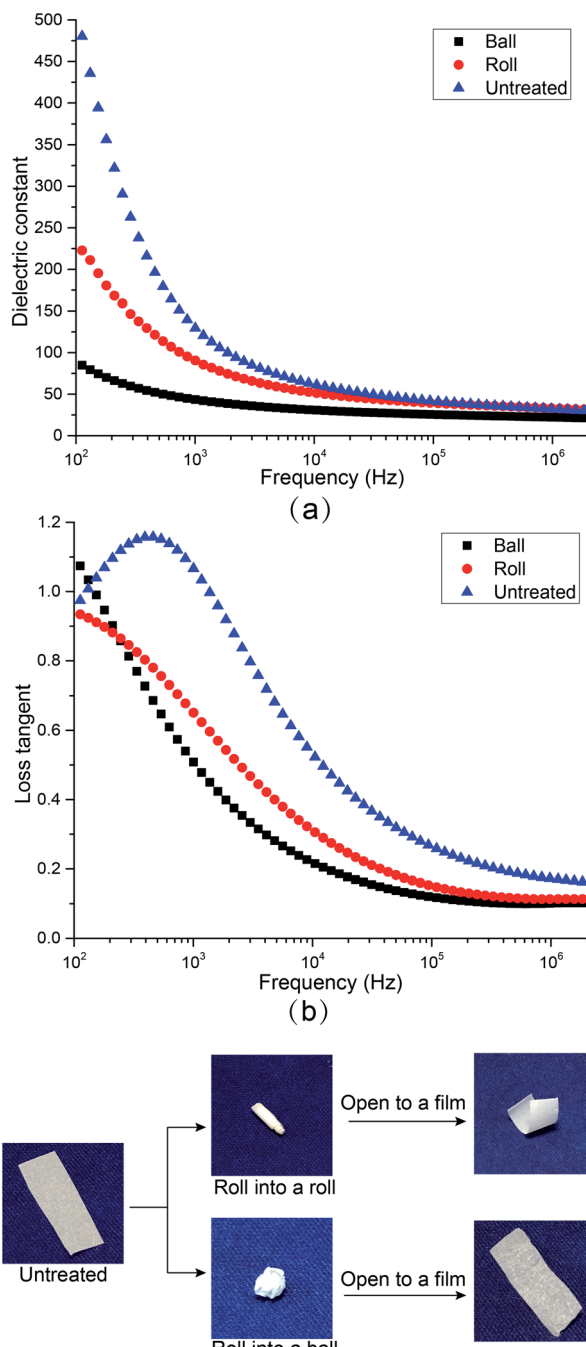


Fig. 5 The influences of rolling treatments on (a) dielectric constant and (b) loss tangent of CNF/BTO nanocomposite films.

loss ( $T_{5\%}$ ) is considered as the start signal of degradation. CNF/BTO (30 wt%) nanocomposite has a  $T_{5\%}$  of  $284\text{ }^{\circ}\text{C}$ , which is slightly higher than that of pure CNF ( $265\text{ }^{\circ}\text{C}$ , Fig. SI 7†). It means that the doping of BTO makes an improvement in thermal stability. The second degradation step located in the temperature range from  $250\text{ }^{\circ}\text{C}$  to  $400\text{ }^{\circ}\text{C}$ , where there is a drastic drop of weight, combined with a DTG peak at  $340\text{ }^{\circ}\text{C}$  and a DSC endothermal peak at  $325\text{ }^{\circ}\text{C}$ . This dramatic drop is due to the decomposition of CNF.

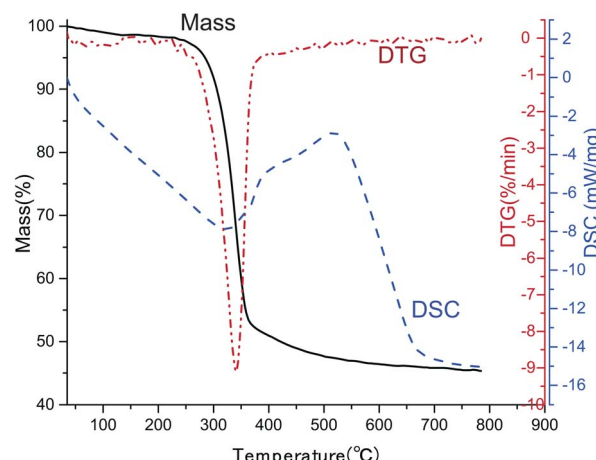


Fig. 6 TGA-DSC curves of CNF/BTO (30 wt%) nanocomposite film.

## Conclusions

A series of high dielectric nanocomposite films based on zero-dimensional tetragonal BTO and three-dimensional CNF were prepared by casting method in aqueous solution. No organic solvents were involved during the preparation, which illustrates the environmental friendliness of the composites. BTO had good distribution within the CNF matrix in the lower range of filler content. The high amount of BTO particles resulted in a porous structure, which led to the drop of dielectric constant. The  $\epsilon_r$  of CNF/BTO composite films reached its maximum value of 188.03 with 30 wt% of BTO, which was more than seven times higher than that of pure CNF, whose  $\epsilon_r$  was 25.24 (at 1 kHz). Meanwhile, the  $\tan \delta$  was only slightly grown from 0.70 to 1.21 (at 1 kHz). The thin film keeps its dielectric properties on an acceptable level even after the twisting treatments. The presence of BTO helps to improve the thermal stability of the composite films. More efforts still need to be made to cut down the remanent polarization and improve the compatibility between the BTO filler and CNF matrix. However, the excellent properties of CNF/BTO composite film demonstrate its great potential to be utilized as a green candidate for HDMs in the field of energy storage.

## Conflicts of interest

There are no conflicts to declare.

## Acknowledgements

The authors acknowledge assistance from the Analytical and Testing Center of Wuhan University for XRD measurements.

## References

- 1 G. Manika and G. Psarras, *eXPRESS Polym. Lett.*, 2019, **13**, 749–758.
- 2 K. Bormanis, A. Kalvane, A. Burkhanov, L. Eglite and R. Dikov, *Ferroelectrics*, 2019, **538**, 12–19.



3 Y. Jiao, L. Deng, S. Yang and P. Zhang, *J. Appl. Polym. Sci.*, 2019, **136**, 47254.

4 L. Hu, J. Zhong, Y. Tian, X. Zheng, J. Cheng and Z. Pu, *J. Mater. Sci.: Mater. Electron.*, 2019, **30**, 221–229.

5 X. Zhang, Y. Wang, Y. Sheng, H. Ye, L. Xu and H. Wu, *Chem. Phys. Lett.*, 2019, **723**, 89–95.

6 M. Panda, A. Mishra and P. Shukla, *SN Appl. Sci.*, 2019, **1**, 230.

7 P. Beena and H. Jayanna, *Polym. Polym. Compos.*, 2019, **27**, 619–625.

8 T. Sebastian, A. Michalek, M. Hedayati, T. Lusiola and F. Clemens, *J. Eur. Ceram. Soc.*, 2019, **39**, 3716–3721.

9 W. Li, M. Chen, Y. Yang, D. Yuan, Y. Ren and X. Cai, *J. Appl. Polym. Sci.*, 2019, **136**, 47447.

10 M. D. Waugh, *Electron. Eng. Times*, 2010, 34–36.

11 M. L. Hassan, A. F. Ali, A. H. Salama and A. M. Abdel-Karim, *J. Phys. Org. Chem.*, 2019, **32**, e3897.

12 L. Zhang, Y. Wang, M. Xu, W. Wei and Y. Deng, *ACS Appl. Energy Mater.*, 2019, **2**, 5945–5953.

13 J. Fu, Y. Hou, M. Zheng and M. Zhu, *J. Mater. Sci.*, 2018, **53**, 7233–7248.

14 J. Fu, Y. Hou, M. Zheng, Q. Wei, M. Zhu and H. Yan, *ACS Appl. Mater. Interfaces*, 2015, **7**, 24480–24491.

15 P. Hu, Y. Shen, Y. Guan, X. Zhang, Y. Lin, Q. Zhang and C. W. Nan, *Adv. Funct. Mater.*, 2014, **24**, 3172–3178.

16 X. Zhang, J. Jiang, Z. Shen, Z. Dan, M. Li, Y. Lin, C. W. Nan, L. Chen and Y. Shen, *Adv. Mater.*, 2018, **30**, 1707269.

17 C. Nawanal, W. Makcharoen, K. Khaosa-Ard, T. Maluangnont, W. Vittayakorn, D. Isarakorn and N. Vittayakorn, *Integr. Ferroelectr.*, 2019, **195**, 46–57.

18 B. Jiang, J. Iocozzia, L. Zhao, H. Zhang, Y.-W. Harn, Y. Chen and Z. Lin, *Chem. Soc. Rev.*, 2019, **48**, 1194–1228.

19 R. Popielarz, C. Chiang, R. Nozaki and J. Obrzut, *Macromolecules*, 2001, **34**, 5910–5915.

20 L. Gao, Q. Liu, Z. Gao and Y. Lin, *Polym. Compos.*, 2008, **29**, 1160–1164.

21 Z. Li, L. A. Fredin, P. Tewari, S. A. DiBenedetto, M. T. Lanagan, M. A. Ratner and T. J. Marks, *Chem. Mater.*, 2010, **22**, 5154–5164.

22 P. Saini, M. Arora, G. Gupta, B. K. Gupta, V. N. Singh and V. Choudhary, *Nanoscale*, 2013, **5**, 4330–4336.

23 Q. Li, K. Han, M. R. Gadinski, G. Zhang and Q. Wang, *Adv. Mater.*, 2014, **26**, 6244–6249.

24 X. Zhang, Y. Shen, Q. Zhang, L. Gu, Y. Hu, J. Du, Y. Lin and C. W. Nan, *Adv. Mater.*, 2015, **27**, 819–824.

25 Z.-M. Dang, H.-Y. Wang and H.-P. Xu, *Appl. Phys. Lett.*, 2006, **89**, 112902.

26 Z. M. Dang, Y. Q. Lin, H. P. Xu, C. Y. Shi, S. T. Li and J. Bai, *Adv. Funct. Mater.*, 2008, **18**, 1509–1517.

27 J. Li, J. Claude, L. E. Norena-Franco, S. I. Seok and Q. Wang, *Chem. Mater.*, 2008, **20**, 6304–6306.

28 P. Kim, N. M. Doss, J. P. Tillotson, P. J. Hotchkiss, M.-J. Pan, S. R. Marder, J. Li, J. P. Calame and J. W. Perry, *ACS Nano*, 2009, **3**, 2581–2592.

29 K. Yang, X. Huang, Y. Huang, L. Xie and P. Jiang, *Chem. Mater.*, 2013, **25**, 2327–2338.

30 P. Kim, S. C. Jones, P. J. Hotchkiss, J. N. Haddock, B. Kippelen, S. R. Marder and J. W. Perry, *Adv. Mater.*, 2007, **19**, 1001–1005.

31 S. Luo, Y. Shen, S. Yu, Y. Wan, W.-H. Liao, R. Sun and C.-P. Wong, *Energy Environ. Sci.*, 2017, **10**, 137–144.

32 Y. Wang, J. Cui, Q. Yuan, Y. Niu, Y. Bai and H. Wang, *Adv. Mater.*, 2015, **27**, 6658–6663.

33 Q. Chen, Y. Shen, S. Zhang and Q. Zhang, *Annu. Rev. Mater. Res.*, 2015, **45**, 433–458.

34 X. Huang and P. Jiang, *Adv. Mater.*, 2015, **27**, 546–554.

35 T. V. Prateek and R. Gupta, *Chem. Rev.*, 2016, **116**, 4260–4317.

36 X. Zhang, Y. Shen, B. Xu, Q. Zhang, L. Gu, J. Jiang, J. Ma, Y. Lin and C. W. Nan, *Adv. Mater.*, 2016, **28**, 2055–2061.

37 Y. Hao, X. Wang, K. Bi, J. Zhang, Y. Huang, L. Wu, P. Zhao, K. Xu, M. Lei and L. Li, *Nano Energy*, 2017, **31**, 49–56.

38 Z. Pan, L. Yao, J. Zhai, D. Fu, B. Shen and H. Wang, *ACS Appl. Mater. Interfaces*, 2017, **9**, 4024–4033.

39 E. D. Cranston and D. G. Gray, *Biomacromolecules*, 2006, **7**, 2522–2530.

40 R. J. Moon, G. T. Schueneman and J. Simonsen, *JOM*, 2016, **68**, 2383–2394.

41 W. Yang, L. Jiao, W. Liu and H. Dai, *Nanomaterials*, 2019, **9**, 107.

42 J. Tao, S.-a. Cao, W. Liu and Y. Deng, *Cellulose*, 2019, **26**, 6087–6098.

43 N. Madusanka, S. G. Shivareddy, M. D. Eddleston, P. Hiralal, R. A. Oliver and G. A. Amaralunga, *Carbohydr. Polym.*, 2017, **172**, 315–321.

44 H. Y. Choi and Y. G. Jeong, *Compos. B Eng.*, 2019, **168**, 58–65.

45 A. El Sayed and S. El-Gamal, *J. Polym. Res.*, 2015, **22**, 97.

46 S. K. Mahadeva, K. Walus and B. Stoeber, *ACS Appl. Mater. Interfaces*, 2014, **6**, 7547–7553.

47 X. L. Zeng, L. B. Deng, Y. M. Yao, R. Sun, J. B. Xu and C. P. Wong, *J. Mater. Chem. C*, 2016, **4**, 6037–6044.

48 Y. B. Pottathara, V. Bobnar, M. Finšgar, Y. Grohens, S. Thomas and V. Kokol, *Polymer*, 2018, **147**, 260–270.

49 Y. Pottathara, S. Thomas, N. Kalarikkal, T. Griesser, Y. Grohens, V. Bobnar, M. Finšgar, V. Kokol and R. Kargl, *New J. Chem.*, 2019, **43**, 681–688.

50 M. Mohiuddin, K. K. Sadasivuni, S. Mun and J. Kim, *RSC Adv.*, 2015, **5**, 34432–34438.

51 Y. Beeran, V. Bobnar, S. Gorgieva, Y. Grohens, M. Finšgar, S. Thomas and V. Kokol, *RSC Adv.*, 2016, **6**, 49138–49149.

52 T. Inui, H. Koga, M. Nogi, N. Komoda and K. Suganuma, *Proceedings of the 14th IEEE International Conference on Nanotechnology*, Toronto, Canada, 2014.

53 S. Ji, J. Jang, E. Cho, S. H. Kim, E. S. Kang, J. Kim, H. K. Kim, H. Kong, S. K. Kim and J. Y. Kim, *Adv. Mater.*, 2017, **29**, 1700538.

54 S. D. Milovidova, O. V. Rogazinskaya, A. S. Sidorkin, N. H. Thuong, E. V. Grohotova and N. G. Popravko, *Ferroelectrics*, 2014, **469**, 116–119.

55 K. T. Nguen, S. Milovidova, A. Sidorkin and O. Rogazinskaya, *Phys. Solid State*, 2015, **57**, 503–506.

56 H. Nguyen, A. Sidorkin, S. Milovidova and O. Rogazinskaya, *Ferroelectrics*, 2016, **501**, 180–186.



57 H. Nguyen, A. Sidorkin, S. Milovidova and O. Rogazinskaya, *Ferroelectrics*, 2016, **498**, 27–35.

58 D. Y. Liu, G. Sui and D. Bhattacharyya, *Compos. Sci. Technol.*, 2014, **99**, 31–36.

59 C. Yang, C. Chen, Y. Pan, S. Li, F. Wang, J. Li, N. Li, X. Li, Y. Zhang and D. Li, *Electrochim. Acta*, 2015, **182**, 264–271.

60 V. Anju and S. K. Narayanan, *AIP Adv.*, 2016, **6**, 015109.

61 S. P. Raghunathan, S. Narayanan, A. C. Poulose and R. Joseph, *Carbohydr. Polym.*, 2017, **157**, 1024–1032.

62 A. Kafy, K. K. Sadasivuni, H. C. Kim, A. Akther and J. Kim, *Phys. Chem. Chem. Phys.*, 2015, **17**, 5923–5931.

63 C. Chiang and R. Popielarz, *Ferroelectrics*, 2002, **275**, 1–9.

64 C. Jia, Z. Shao, H. Fan and J. Wang, *RSC Adv.*, 2015, **5**, 15283–15291.

65 M. Nogi, S. Iwamoto, A. N. Nakagaito and H. Yano, *Adv. Mater.*, 2009, **21**, 1595–1598.

66 D. Klemm, F. Kramer, S. Moritz, T. Lindstrom, M. Ankerfors, D. Gray and A. Dorris, *Angew. Chem., Int. Ed. Engl.*, 2011, **50**, 5438–5466.

67 B. Poyraz, A. Tozluoglu, Z. Candan and A. Demir, *J. Polym. Eng.*, 2017, **37**, 921–931.

68 Y. Fujisaki, H. Koga, Y. Nakajima, M. Nakata, H. Tsuji, T. Yamamoto, T. Kurita, M. Nogi and N. Shimidzu, *Adv. Funct. Mater.*, 2014, **24**, 1657–1663.

69 X. Du, Z. Zhang, W. Liu and Y. Deng, *Nano Energy*, 2017, **35**, 299–320.

70 A. M. Abdel-karim, A. H. Salama and M. L. Hassan, *J. Phys. Org. Chem.*, 2018, **31**, e3851.

71 U. Celano, K. Nagashima, H. Koga, M. Nogi, F. Zhuge, G. Meng, Y. He, J. De Boeck, M. Jurczak and W. Vandervorst, *NPG Asia Mater.*, 2016, **8**, e310.

72 A. Kafy, K. K. Sadasivuni, A. Akther, S.-K. Min and J. Kim, *Mater. Lett.*, 2015, **159**, 20–23.

73 Y. Li, M. Misra and S. Gregori, *IET Circuits, Devices Syst.*, 2017, **11**, 638–647.

74 A. Petritz, A. Wolfberger, A. Fian, T. Griesser, M. Irimia-Vladu and B. Stadlober, *Adv. Mater.*, 2015, **27**, 7645–7656.

75 Z. Lu, W. Hu, F. Xie and Y. Hao, *Cellulose*, 2017, **24**, 2827–2835.

76 X. An, D. Cheng, L. Dai, B. Wang, H. J. Ocampo, J. Nasrallah, X. Jia, J. Zou, Y. Long and Y. Ni, *Appl. Catal. B Environ.*, 2017, **206**, 53–64.

77 H. Lu, L. Zhang, B. Wang, Y. Long, M. Zhang, J. Ma, A. Khan, S. P. Chowdhury, X. Zhou and Y. Ni, *Cellulose*, 2019, **26**, 4909–4920.

78 Y. Zhao, W. Dang, L. Si and Z. Lu, *Cellulose*, 2019, **26**, 2035–2046.

79 A. F. Ali, M. L. Hassan, A. A. Ward and E. M. El-Giar, *Polym. Compos.*, 2017, **38**, 893–907.

80 S. Kamel, A. A. Haroun, A. M. El-Nahrawy and M. A. Diab, *J. Renewable Mater.*, 2019, **7**, 193–203.

81 H. Xu and L. Gao, *J. Am. Ceram. Soc.*, 2003, **86**, 203–205.

82 F.-S. Yen, H.-I. Hsiang and Y.-H. Chang, *Jpn. J. Appl. Phys.*, 1995, **34**, 6149.

83 C. Jia, Z. Shao, H. Fan, R. Feng, F. Wang, W. Wang, J. Wang, D. Zhang and Y. Lv, *Composites, Part A*, 2016, **86**, 1–8.

84 S. Emmert, M. Wolf, R. Gulich, S. Krohns, S. Kastner, P. Lunkenheimer and A. Loidl, *Eur. Phys. J. B*, 2011, **83**, 157–165.

85 H. B. Lu and X. Y. Zhang, *J. Appl. Phys.*, 2006, **100**, 054104.

86 M. Samet, V. Levchenko, G. Boiteux, G. Seytre, A. Kallel and A. Serghei, *J. Chem. Phys.*, 2015, **142**, 194703.

87 M. Abutalib, *Phys. B*, 2019, **557**, 108–116.

88 T. Tanaka, M. Kozako, N. Fuse and Y. Ohki, *IEEE Trans. Dielectr. Electr. Insul.*, 2005, **12**, 669–681.

89 M. Beztout, A. Boukerrou, H. Djidjelli, C. Barres and F. Fenouillot, *Cellul. Chem. Technol.*, 2015, **49**, 517–528.